Molecular dynamics simulations of two-step process enable room-temperature synthesis of α-$FAPbI_3$

Paramvir Ahlawat[a], Haizhou Lu[e,f], Amita Ummadisingu[e], Haiyang Niu[b,d], Michele Invernizzi[b,d], Shaik Mohammed Zakeeruddin[e], Anders Hagfeldt*[f], Michael Graetzel*[e], Ursula Rothlisberger*[a], and Michele Parrinello*[b,d]

[a]Laboratory of Computational Chemistry and Biochemistry, Ecole Polytechnique Fédérale de Lausanne, CH-1015 Lausanne, Switzerland; [b]Institute of Computational Science, Università della Svizzera Italiana, Ch-6900 Lugano, Switzerland; [d]Department of Chemistry and Applied Biosciences, Eidgenossische Technische Hochschule (ETH) Zurich; [e]Laboratory of Photonics and Interfaces, Ecole polytechnique Fédérale (EPFL) de Lausanne, Lausanne, Switzerland, CH-1015; [f]Laboratory of Photomolecular Science, Ecole polytechnique Fédérale (EPFL) de Lausanne, Lausanne, Switzerland, CH-1015

It is well established that the lack of understanding the crystallization process in two-step sequential deposition has a direct impact on efficiency, stability and reproducibility of perovskite solar cells. Here, we try to understand the solid-solid phase transition occuring during two-step sequential deposition of methylammonium lead iodide and formamidinium lead iodide. Using metadynamics, X-ray diffraction and Raman spectroscopy, we reveal the microscopic details of this process. We find that the formation of perovskite proceeds through intermediate structures and report polymorphs found for methylammonium lead iodide and formamidinium lead iodide. From simulations, we discover a possible crystallization pathway for the highly efficient metastable α-phase of formamidinium lead iodide. Guided by these simulations, we perform experiments that results in the room temperature crystallization of α-formamidinium lead iodide.

Halide Perovskites | Enhanced sampling - Metadynamics | Crystallization | Intermediate phases | $MAPbI_3$ | α-$FAPbI_3$ | X-ray diffraction | Raman spectroscopy

Perovskite solar cells (PSCs) are one of the most promising and cheap photovoltaic devices(1). However, their widespread application is made difficult by several technological problems related to their long-term stability and processability.

Two-step deposition(2) is one of the main experimental techniques used to fabricate highly efficient and stable PSCs (3, 4). In this process, lead iodide (PbI_2) is deposited first and then converted to perovskite by adding halide salts of monovalent cations such as methylammonium iodide (MAI) and formamidinium iodide (FAI)(5). This process offers several advantages for industrial-scale fabrication(6–8) of larger modules relative to the single-step spin-coating technology which is limited to smaller devices. However when scaling up, maintaining reproducible high performances and long-term stability is difficult. These problems arise mainly from the lack of control over the fabrication process (9, 10). Therefore, it is essential to understand at the atomic-level the mechanism of halide perovskites crystallization.

Among the several perovskites of interest, we study here the two-step fabrication of methylammonium lead iodide ($MAPbI_3$) and formamidinium lead iodide ($FAPbI_3$). The first one is a well studied system on which many experiments have been performed. The second $FAPbI_3$, is a compound that in its α-$FAPbI_3$ polymorph, a compound that has several attractive features like a $\sim$1.45 eV bandgap, high charge carrier mobility and stability. The practical application of α-$FAPbI_3$ has been hampered by the fact that the α-phase is metastable and the thermodynamic phase transition requires high temperatures at $\sim$150°C. We anticipate here that the main result of this paper is the discovery of a low temperature pathway to the fabrication of α-$FAPbI_3$. This has been made possible by a combined experimental and theoretical effort that has uncovered the microscopic details of the crystallization process.

Previous experimental research (11–20) on $MAPbI_3$ has revealed that the two-step process occurs via intercalation of the MA^+ cations in the PbI_2 layers followed by a transformation to the perovskite structure via intermediate phases.

However, these experiments could not resolve the nature of intermediate phases nor elucidate the underlying atomistic mechanism. In order to fill in the details that experiments cannot resolve and obtain an understanding of the microscopic transformation mechanism, we have performed a molecular dynamics investigation. Since the time scale involved in the fabrication process is too large, we have made use of an enhanced sampling technique. In particular, we have used well-tempered metadynamics (WTMetaD)(21, 22). This method allows simulating processes that take place on an extended time scale with affordable computing resources.

We started by an experimental characterization of

*To whom correspondence should be addressed.
ursula.roethlisberger@epfl.ch, anders.hagfeldt@epfl.ch, michael.graetzel@epfl.ch, michele.parrinello@phys.chem.ethz.ch

$MAPbI_3$ via X-ray and Raman scattering. These experiments provided additional evidence that the picture of the initial intercalation followed by a sequence of intermediates states is correct. We then performed WTMetaD simulations and found that transformation from the intercalated initial structure (see Figure 3a) to the final perovskite arrangement takes place via a sequence of intermediates (see Figure 3b-d). These theoretical results are in line with present and past experiments (23–27).

The highly satisfactory agreement between theory and experiments in the case of $MAPbI_3$ encouraged us to investigate theoretically whether a similar process was operational also for the much less studied α-$FAPbI_3$. This time we started from simulations and indeed discovered that a two-step process is possible at lower temperatures. This was then followed by experiments that confirmed the outcome of the simulations and enabled the low-temperature formation of α-$FAPbI_3$.

Results

XRD and Raman Spectroscopy. The formation of $MAPbI_3$ in the sequential deposition method was monitored using XRD measurements by examining various samples at different reaction times. See Methods for details about sample preparation.

The XRD spectra of these samples and an unreacted control sample of PbI_2 are shown in Supplementary Figure S1a. During the initial seconds of the sequential deposition, we observe a sharpening and narrowing of the (001) peak as the crystallinity of the PbI_2 increases, similar to our previous work(28–30). As the reaction progresses, the peak widens becoming less sharp. We further analyzed this process computationally. First we construct models with different size supercells of PbI_2 with an increasing number of layers in the (001) direction, depicted in Supplementary Figure S2. We then compute the XRD spectra of these supercells, shown in Supplementary Figure S3 and compare them with the experimental XRD spectra, see Supplementary Figure S1b. We find that during the initial seconds of the dipping, layers of edge-sharing PbI_6 octahedra stack over each other in (001) direction of crystalline PbI_2. We attribute this fact to intercalation commencing before the formation of $MAPbI_3$. These XRD measurements have provided an interesting first global view of the process.

Next we collected Raman spectra for monitoring the progress of $MAPbI_3$ formation in the sequential deposition reaction. All the Raman spectra are shown in Figure 1. The details are discussed in the Methods section. Here we take a closer look at the peaks at 140 and 143cm^{-1}, which are associated with the rotational motion of the methylammonium ion in $MAPbI_3$(20).

The intercalation of the MA^+ ion into the lattice causes the appearance of the peak at 140cm^{-1} at early stages of the reaction (Figure1b, 15s), which then shifts towards 143cm^{-1} around 30s while growing in intensity. The sig-

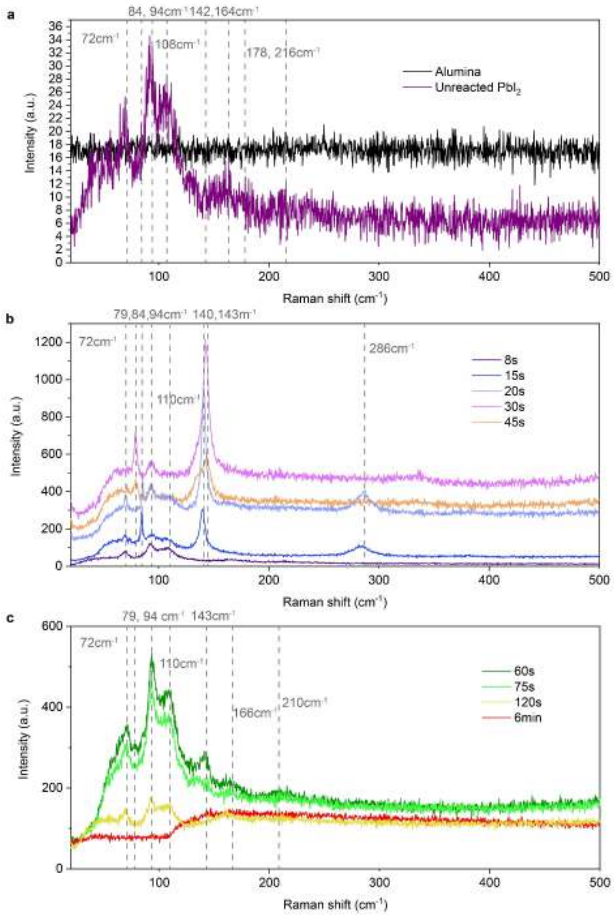

Fig. 1. Raman spectra monitoring the progress of $MAPbI_3$ formation in the sequential deposition reaction. a) Control measurements of the alumina scaffold on glass substrate and the unreacted PbI_2 film. b) samples reacted in 5mg/ml MAI solution after 8, 15, 20, 30 and 45s. c) samples reacted in 5mgml^{-1} MAI solution after 60, 75, 120s and 6min.

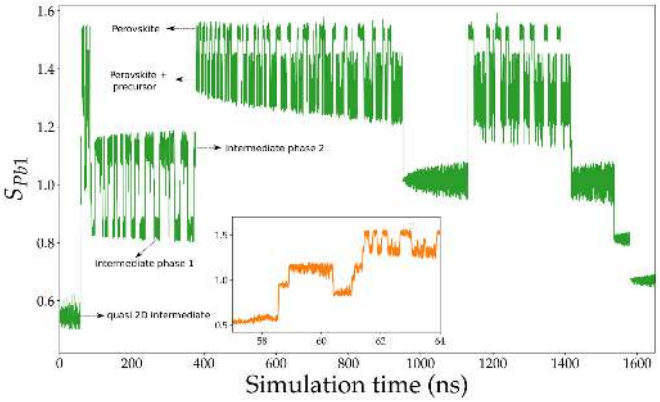

Fig. 2. Structure factor: Evolution of first peak of structure factor of Pb^{2+} ions (S_{Pb1}) with WTmetaD simulation at 370K. Inset is a zoom of S_{Pb1} for the first transition from quasi-2D to 3D.

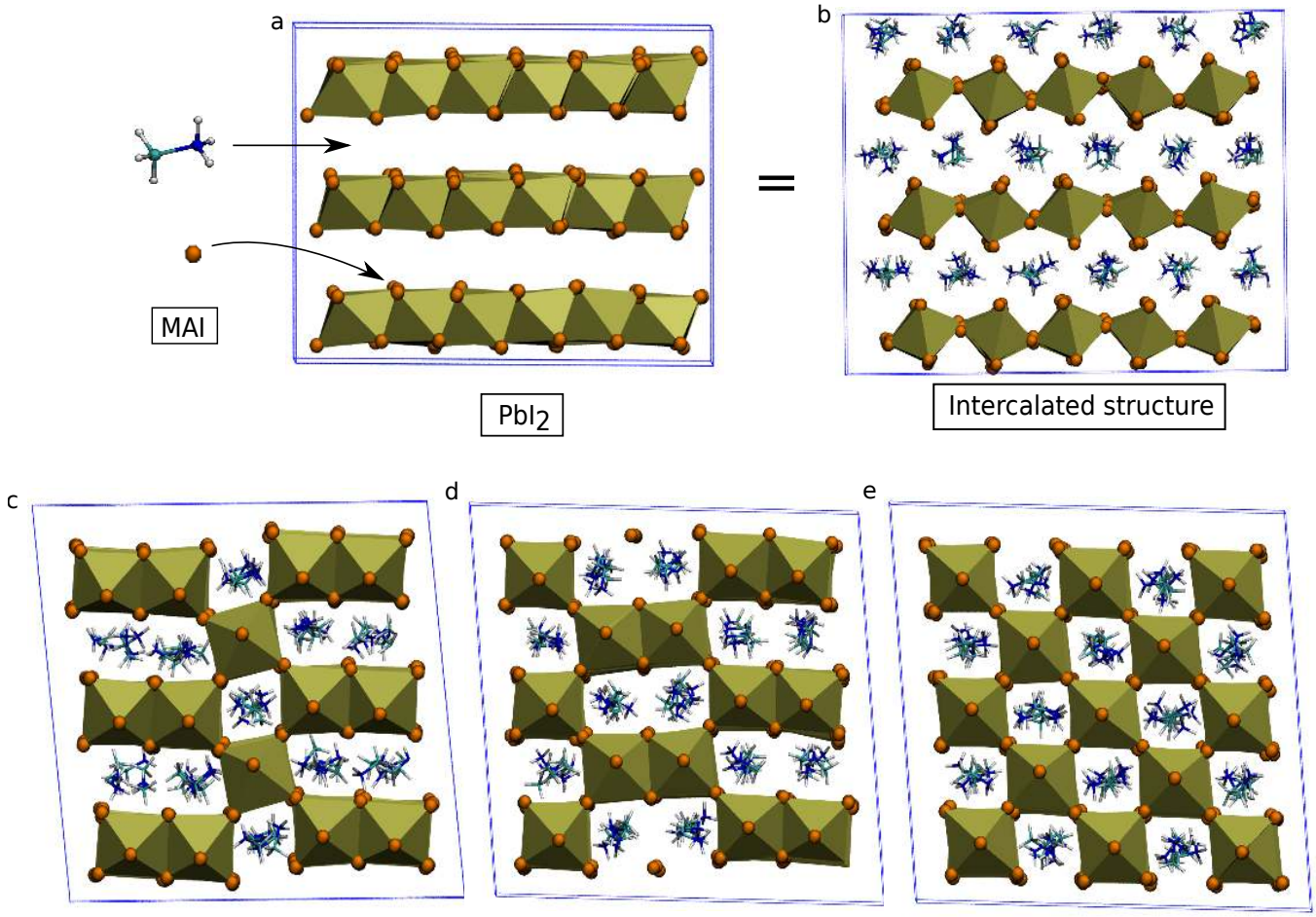

Fig. 3. Phase transition via intermediate phases: Images a and b show the intercalation process. Images b to e display the phase transition from quasi-2D intercalated structure (b) to perovskite phase of $MAPbI_3$ (e). Pb-I complexes are shown as golden polyhedra with Pb^{2+} in the center and I^- as dark orange balls on the corners. MA^+ cations are shown with balls and sticks with carbon as light blue, nitrogen as dark blue and hydrogens being white. Similar structures have been observed for other materials such as $MgSiO_3$, Fe_2O_3, $CsIrO_3$, $AgTaS_3$, $NaMgF_3$, $MgGeO_3$.

nal disappears and broadens at room temperature, as expected for the perovskite structure(31), as the reaction progresses to completion (see data for 75s and 6min). These results are highly consistent with the report by Jain *et al.*(20) who also ascribe these changes to the consumption of PbI_2 and the progress of methylammonium iodide intercalation.

Overall, these findings from the experimental investigation suggest the presence of intermediates in the intercalation of the methylammonium ion into the PbI_2 and the associated structural reorganization that finally results in the formation of the $MAPbI_3$ perovskite in the sequential deposition reaction.

WTmetaD simulations. From the above mentioned experimental findings, we start from the plausible hypothesis that monovalent cations (MA^+) intercalate between the edge-sharing layers of Pb-I octahedra in PbI_2 (Fig. 3a) and form a quasi-2D layered structure. We manually construct such a structure by placing MA^+ ions in between the layers of PbI_2 (Figure 3b). The remaining iodide (I^-) from MAI is placed on the Pb-I octahedra to have a final charge-neutral layered $MAPbI_3$ structure. This model is based on experimentally reported intercalated PbI_2 structures(32, 33). We verify the stability of this structure by carrying out a variable cell enthalpic optimization with classical MD simulations as well as density functional theory (DFT). From both techniques, we find that the structure shown in (Fig. 3b) is stable. Details are presented in the Methods section. Furthermore, we calculate the powder diffraction pattern of the DFT relaxed intercalated structure. We find that the first peak of PbI_2 at $\sim$12.7° shifts to $\sim$11.4° for the intercalated structure, see Supplementary figure S4. This observation is consistent with the previously reported XRD experiments on two-step deposition(34).

We proceed with the WTmetaD simulations of the transformation of the intercalated $MAPbI_3$ to the perovskite. We prepare two different size supercells of the intercalated structure with 32 and 108 formula units of $MAPbI_3$, respectively. With these supercells, we perform WTMetaD simulations as outlined in the Methods section. These simulations are done at different temperatures ranging from 300 to 420K corresponding to typical experimental conditions. For both supercells, we successfully observe the transformation of the starting quasi-2D layered intermediate structure to the 3D corner-sharing perovskite (atomistic views of both simulations are shown in Supplementary Movies M1 and M2). Since a similar transformation mechanism was found in both cases, we only present the results for the larger supercell while the results for the smaller system are given in the SI. Interestingly, we find that the phase transition from quasi-2D to 3D perovskite proceeds through distinct intermediary structures as shown in Figure 3b to e. From these figures and movies: one can see that the intermediate phases are

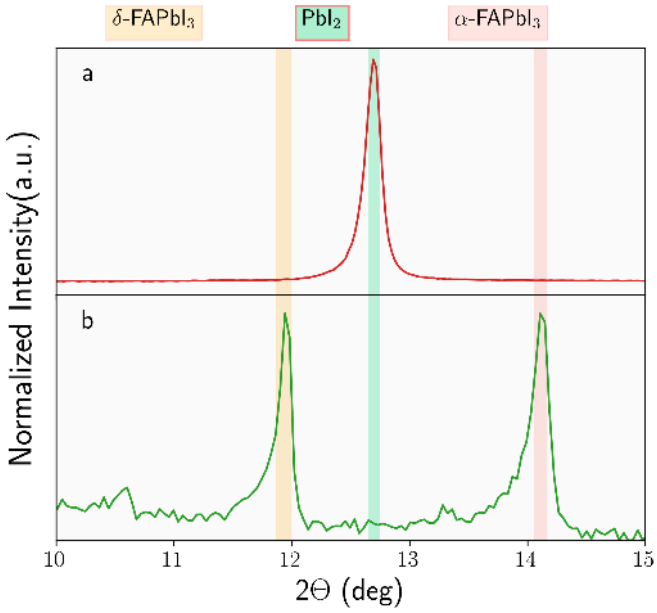

Fig. 4. XRD spectra of $FAPbI_3$ samples: Top panel is the XRD spectrum of PbI_2 deposited film and bottom panel shows the corresponding data after the FAI loaded onto PbI_2 at room temperature.

formed by rotating PbI_6 octahedra over the planes of PbI_2 (along the axis of the Pb-Pb edge-shared octahedra). This is a general way to the formation of intermediate structures. In the larger supercell more PbI_6 octahedra are required to rotate for complete formation of the perovskite structure which leads to formation of more intermediate phases. We quantify this with the evolution of the first peak ($q \approx 10$ nm^{-1} = $2\Theta \approx 14.1°$) of the Debye structure factor (S_{Pb1}) of Pb^{2+} ions in cubic perovskites, detailed in the Methods section. Figure 2 shows the evolution of S_{Pb1} for the larger supercell while results for the smaller supercell are shown in Supplementary Figure S5. Moreover, we further explore the free energy landscape and find a variety of different polymorphic structures. We outline all of the observed phases in Supplementary Figure S6. By performing variable cell enthalpic optimization with DFT, we find that all of the structures are stable, see SI. This polymorphic behavior in halide perovskites is related to the existing polytypism in PbI_2(35, 36), which also gives rise to these intermediates in crystallization. Many of these polymorphs have a high probability of forming during crystallization of other halide perovskite systems and some of these structures have already been identified experimentally.(23–26) Encouraged by the results for $MAPbI_3$, we proceed to study the phase transition of $FAPbI_3$. Here, the main practical challenge is to find the possible pathways for crystallization of the pure samples of the photoactive α phase. We attempt to solve this problem by first performing simulations and then experiments based on insights from the simulations. We carry out simulations similar to the above reported approach for $MAPbI_3$. First, we construct a quasi-2D PbI_2 struc-

ture intercalated with FA^+, similar to the structure in Figure 3b. We perform WTMetaD simulations of two supercells of 32 and 48 formula units of $FAPbI_3$, again , as in the case of $MAPbI_3$, in both cases, we successfully observe the phase transition to the perovskite structure of $FAPbI_3$. An atomic view of this phase transition is shown in Supplementary Movie M3. Remarkably, this simulation reveals a direct path (from the intercalated PbI_2) to the formation of the metastable phase of α-$FAPbI_3$ without the need for a high-temperature induced transformation via the δ phase. In particular, our findings suggest that α-$FAPbI_3$ can be formed at lower temperatures from a quasi-2D structure.

We test this newly found route by directly attempting crystallization of α-$FAPbI_3$ at room temperature. At first, we deposit PbI_2 layer from a PbI_2 solution in N,N-Dimethylformamide (DMF) and Dimethyl sulfoxide (DMSO). After annealing at 70°C, the PbI_2 films are dipped into FAI solution dissolved in isopropanol (IPA) (20mg/ml). FAI loading is done at room temperature inside nitrogen filled glove-box. This experiment is shown in Supplementary movie E1. From the movie E1, one can observe that the yellow phase of PbI_2 directly transforms into the black phase α-$FAPbI_3$. To gain further insights, we perform XRD measurements on the first PbI_2 deposited film and after the loading of FAI. Figure 4 shows that initially PbI_2 has formed as indicated by its characteristic peak at $\sim$12.7°. After FAI loading, we see the formation of cubic(α)-phase of $FAPbI_3$ in addition to formation of δ phase, as indicated by its typical XRD peak $\sim$14.1°. Therefore, it becomes clear that the perovskite structure of $FAPbI_3$ can be formed by FAI intercalation into PbI_2 as predicted from our simulations. To scrutinize this further, we also perform another experiment where we load FAI solution onto PbI_2 layer during spin-coating process. At difference to the two-step sequential deposition, in this process, we do not observe the formation of the black perovskite phase of $FAPbI_3$. This can be due to the fact that the PbI_2-layered structure gets destroyed while spinning the substrate and intercalation of FAI becomes difficult. Further optimization of this process will help in the formation of pure α-$FAPbI_3$ based solar cell modules.

In the end, we point out that the phase transition from a quasi-2D to 3D perovskite structure via rotation of PbI_6 octahedra is a general pathway to form the perovskite structure. This theoretical result can be useful as such a quasi-2D phase can be tailored with additives to synthesize high-quality and stable α-$FAPbI_3$. One example are anion additives such as cloride, which is widely known to modify the crystallization process and has become a commonly used additive to make high efficiency α-$FAPbI_3$ based solar cells. Recent XRD(37) and cryo-electron microscopy (cryo-EM)(38) experiments have shown that chloride induces a quasi-2D like intermediate phase which can help in nucleation of α-$FAPbI_3$. Therefore, the current theoretical approach presented here can be applied to unravel the effects of different additives. Moreover, the reverse phase transition from 3D to quasi-2D might also be present during degradation leading to PbI_2.

Conclusions. By using WTmetaD, we explore the phase transition paths in the two-step deposition of halide perovskites. Combining simulations and experiments, we reveal the intricate details of the phase transition of $MAPbI_3$ and $FAPbI_3$. We find a low temperature crystallization pathway for the α-$FAPbI_3$. Our combined experimental and simulation study will help in designing better industrial scale processing techniques (39) for $MAPbI_3$ and $FAPbI_3$. In the end, we point out that other Raman studies(33, 40) have also demonstrated the PbI_2 intercalation with other organic molecules such as ammonia, ethylamine ($C_2H_5NH_2$), butylamine ($C_4H_9NH_2$), and even larger ones such as cyclohexenyl ethyl ammonium ($C_6H_9C_2H_4NH_3{}^+$). Therefore, our combined experimental and simulations study can be extended to study the formation of other systems such as lower-dimensional (2D) perovskites as well.

Materials and Methods

We use a fixed point charge model for $MAPbI_3$ (41) with 1.0 nm cutoff for nonbonded interactions. We take the PbI_2 parameters from this force field and prepare the force fields for $FAPbI_3$ by mixing rules. In variable cell NPT simulations, this force fields gives stable delta and cubic phases and can also reproduce all other experimentally known 4H and 6H polytypes of $FAPbI_3$. Electrostatics are treated with the particle-particle-particle-mesh Ewald method and the SHAKE algorithm(42) is used to constrain covalent bonds to hydrogen. All systems are simulated with the Large-scale Atomic/Molecular Massively Parallel Simulator(LAMMPS) code (31 Mar 2017)(43). We first minimize all systems with a conjugate gradient algorithm keeping a tolerance of maximum force of 10^{-3} kcal/molA. After minimization, we perform a 100ps NVT equilibration run. All production run simulations presented in this work were carried out in the isothermal-isobaric ensemble with a velocity re-scaling thermostat (44) of relaxation time 0.1 ps and a Parrinello-Rahman barostat (45). All WTmetaD simulations are performed with PLUMED 2.4 (46).

DFT calculations. We use Quantum Espresso (47) for geometry optimization with Generalized Gradient Approximation (GGA) of Kohn-Sham DFT, namely the Perdew-Burke-Ernzerhof (PBE) functional revised for solids(PBEsol)(48). For the layered structures, we use the PBE functional(49) with Grimme D2(50) dispersion corrections for van der Waals interactions. In all DFT calculations, we use ultra-soft pseudo-potentials with a plane wave basis set of 60 Ry kinetic energy cutoff and 420 Ry density cutoff. All structure files are reported in the SI.

Collective variables. In this study we use an experimentally measurable quantity, the structure factor (51) as a collective

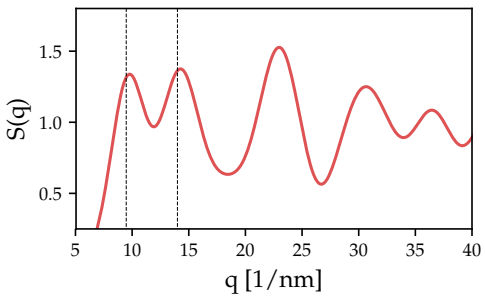

Fig. 5. Debye structure factor of Pb^{2+} ions in cubic phase of $MAPbI_3$. MA^+ have a similar profile due to the symmetry of the cubic phase.

variable (CV). In particular we employ the Debye form (52) of structure factor (S(q)):

$$S(q) = 1 + \frac{1}{N}\sum_{i=1}^{N}\sum_{j\neq i}^{N}\frac{sin(qr_{\mathrm{ij}})}{qr_{\mathrm{ij}}} \quad [1]$$

In this equation the sum is done over neighbors of atom i which are contained in a sphere of radius r_c. As previously done we have added a damping function to remove the termination effects from a finite cutoff. Further details are provided in Refs. (51). However, contrary to previous applications, perovskites are multicomponent systems. In order to deal with this, we use a linear combination of the first two peaks of the structure factors of individual species Pb^{2+} and MA^+, as shown in Figure 5. We design this CV based on two main factors: (a) Pb^{2+} are the heaviest atoms and contribute most to XRD spectra and (b) our previous simulations (53) have revealed that the monovalent cations (MA^+ and FA^+) play an important role in the crystallization process of halide perovskite. Furthermore, these are also the peaks which are assigned to identify perovskite formation in GIWAX experiments. We represent the MA^+ and FA^+ cations with the center of C-N bond similar to our previous study (53).

$$CV = S_{\mathrm{Pb1}} + S_{\mathrm{Pb2}} + S_{\mathrm{MA1}} + S_{\mathrm{MA2}} \quad [2]$$

We use this CV to perform the phase transition from the quasi-2D phase to 3D-perovskite. In this study, we have focused on the phase transition of halide perovskites. A similar methodology can also be used to study the phase transitions in many other perovskites systems such as $MgSiO_3$(54) which is important for earth seismic activities and perovskite solid electrolytes which are promising materials for next-generation Li^+ ion solid-state batteries (55).

Experimental Methods:.

Sample preparation:. $MAPbI_3$ samples were prepared first by depositing a PbI_2 layer directly on glass substrates for the XRD measurements. Samples used for the Raman spectroscopy were made on glass with a mesoporous layer of 23nm particles of alumina on them. A 1.3M PbI_2 solution in DMF was spin coated and the film was then heated at 70 °C for 10 min. This was followed by the reaction with 5mg/ml methylammonium iodide in isopropanol at room temperature, where the sample was dipped in the solution for different periods of time. The final steps were washing in pure isopropanol to halt the reaction and heating at 70 °C for 10 min.

For $FAPbI_3$ samples, 1.3M PbI_2 solution (DMF:DMSO = 9:1) was spin coated at a speed of 2000 rpm/min for 30 seconds. Then, the PbI_2 layer was annealed at 70 degree C for 1 minute. After that, the PbI_2 layer was dipped inside a IPA solution of FAI (20 mg/mL) for different times.

XRD experiments:. XRD data is measured in the Bragg-Brentano geometry using a Bruker D8 Advance powder X-ray diffractometer. The setup has Cu Kα (λ= 1.54Å) radiation and operates in reflection, theta-theta mode (fixed sample) with a 2D strip detector. A beam mask of 1cm was chosen to suitably irradiate the films being measured. A step size of 0.01° was used for measurement and time/step was 0.15s.

Raman spectroscopy:. Raman spectroscopy was conducted on a HORIBA LabRAM HR Raman spectrometer. A 532nm green laser was used for excitation. The focal spot size was about 10μm using a 50x long working distance objective. Previous reports(56) have demonstrated the degradation of the perovskite into PbI_2 under high laser intensities. A neutral density filter (OD 3.0) was used to attenuate the laser intensity to avoid damage to the sample.

Raman spectra were collected for monitoring the progress of $MAPbI_3$ formation in the sequential deposition reaction. Figure 1a shows spectra for control samples of the alumina scaffold on the glass substrate and an unreacted PbI_2 film. Figure 1b shows spectra for samples reacted in 5mg/ml MAI solution for 8, 15, 20, 30 and 45s, while Figure 1c shows those for samples reacted for 60, 75, 120s and 6min.

Figure 1a shows that the control measurement on the substrate shows no peaks in the range of interest so its contribution to the Raman signal in the rest of the measurements can be neglected under similar measurement conditions. The 2H polytype of PbI_2 has only three atoms in each unit cell giving rise to 9 degrees of vibrational motion. The spectrum for the unreacted PbI_2 sample shows that peaks at 72cm^{-1} (a doubly degenerate E_g band) and 94cm^{-1} (a symmetric stretch A_{1g}) due to the shearing motion of two iodine layers are present as expected. Additional peaks expected for PbI_2 nanoparticles are detected at 84 and 108cm^{-1}. Peaks that are double in energy of 72, 84, 94 and 108cm^{-1} absorptions are also observed at 142, 164, 178 and 216cm^{-1} and attributed to the overtones of the fundamentals(57).

Now we discuss the Raman spectra of samples reacted with methylammonium iodide. These samples are firstly expected to show indications of the intercalation of the methylammonium ion into the PbI_2 lattice as discussed in the XRD results, followed by structural reorganization to form the perovskite. In the Raman spectra for the hybrid perovskite of interest, due to the considerable difference in mass between the organic and inorganic constituents, the spectral features at different energies are associated with different dynamic processes in the perovskite lattice. The features observed at energies below 200 cm^{-1} are ascribed to a combination of Pb-I cage modes and the associated coupled motion of the MA^+ ions. Those signals above 200cm^{-1} are assigned to the molecular vibrations of the cations(5). However, in the data shown in Figure 1c for a sample reacted for 6 min, consisting of fully reacted perovskite in the tetragonal phase, very few features are distinguishable as anticipated at room temperature(31). Nevertheless, the

data set consisting of the remaining samples shows interesting changes, particularly at energies below 200cm^{-1}, as the formation of perovskite progresses.

Figure 1b shows the intensification of the peak at 79cm^{-1} corresponding to the perturbed asymmetric breathing mode of a $(MAPbI_3)_4$ cluster with reaction time(20). It also shows a sharp peak at 84cm^{-1} at 30s which weakens at 45s, while the peak at 94cm^{-1} strengthens as the reaction progresses beyond this point. From DFT calculations reported in the literature(20), the former can be assigned to the symmetric breathing mode of the PbI_6 octahedra and the latter to the perturbed symmetric breathing mode of a $(MAPbI_3)_4$ cluster. These peaks, particularly the Pb-I breathing mode at 94cm^{-1}, vanish as the perovskite formation reaction progresses (Figure 1c, see data for 75s, 120s and 6min).

Acknowledgements. PA is sincerely thankful to Prof. David Mitzi and Prof. Costas Stoumpos for highly insightful discussions. This research is funded by Swiss National Science Foundation through the NCCR MUST and individual grant 200020-185092. M.P. acknowledge funding from European Union Grant No. ERC-2014-AdG-670227/VARMET. The computational time for this work was provided by the SCITAS supercomputers at EPFL and CSCS, the Swiss National Supercomputing Centre.

Author Contributions. PA conceived and conceptualized research. PA designed and perfomed all the simulations. AU designed and performed experiments on $MAPbI_3$. PA and HL designed and peformed experiments on $FAPbI_3$. PA, HN, MI and MP developed new anaytical tools and analyzed simulations data. UR, SMZ, AH, MG and MP guided research. PA and MP wrote the first draft. All authors discussed the results and wrote the manuscript.

Conflict of Interest. The authors declare no conflict of interest.

Note. AU is currently affiliated with Department of Physics, Cavendish Laboratory, Cambridge, UK. Haiyang Niu is currently affiliated with State Key Laboratory of Solidification Processing, International Center for Materials Discovery, School of Materials Science and Engineering, Northwestern Polytechnical University, Xian 710072, P.R. China.

1. Kojima A, Teshima K, Shirai Y, Miyasaka T (2009) Organometal halide perovskites as visible-light sensitizers for photovoltaic cells. *Journal of the American Chemical Society* 131(17):6050–6051.
2. Burschka J, et al. (2013) Sequential deposition as a route to high-performance perovskite-sensitized solar cells. *Nature* 499(7458):316–319.
3. Jiang Q, et al. (2019) Surface passivation of perovskite film for efficient solar cells. *Nature Photonics* 13(7):460–466.
4. Yang WS, et al. (2017) Iodide management in formamidinium-lead-halide-based perovskite layers for efficient solar cells. *Science* 356(6345):1376–1379.
5. Liang K, Mitzi DB, Prikas MT (1998) Synthesis and characterization of organic- inorganic perovskite thin films prepared using a versatile two-step dipping technique. *Chemistry of materials* 10(1):403–411.
6. Razza S, et al. (2015) Perovskite solar cells and large area modules (100 cm2) based on an air flow-assisted pbi2 blade coating deposition process. *Journal of Power Sources* 277:286–291.
7. Li P, et al. (2018) Inkjet manipulated homogeneous large size perovskite grains for efficient and large-area perovskite solar cells. *Nano Energy* 46:203–211.
8. Park NG, Zhu K (2020) Scalable fabrication and coating methods for perovskite solar cells and solar modules. *Nature Reviews Materials* pp. 1–18.
9. Minemawari H, et al. (2011) Inkjet printing of single-crystal films. *Nature* 475(7356):364–367.
10. Bi D, et al. (2016) Polymer-templated nucleation and crystal growth of perovskite films for solar cells with efficiency greater than 21%. *Nature Energy* 1(10).
11. Brenner TM, et al. (2016) Conversion of single crystalline pbi2 to ch3nh3pbi3: Structural relations and transformation dynamics. *Chemistry of Materials* 28(18):6501–6510.
12. Guo Y, et al. (2015) Chemical Pathways Connecting Lead(II) Iodide and Perovskite via Polymeric Plumbate(II) Fiber.
13. Patel JB, Milot RL, Wright AD, Herz LM, Johnston MB (2016) Formation Dynamics of CH3NH3PbI3 Perovskite Following Two-Step Layer Deposition. *Journal of Physical Chemistry Letters* 7(1):96–102.
14. Barrit D, et al. (2019) Impact of the solvation state of lead iodide on its two-step conversion to mapbi3: An in situ investigation. *Advanced Functional Materials* 29(47):1807544.
15. Sanches AW, Da Silva MA, Cordeiro NJ, Urbano A, Lourenço SA (2019) Effect of intermediate phases on the optical properties of PbI2-rich CH3NH3PbI3 organic-inorganic hybrid perovskite. *Physical Chemistry Chemical Physics* 21(9):5253–5261.
16. Liu J, et al. (2015) High-Quality Mixed-Organic-Cation Perovskites from a Phase-Pure Non-stoichiometric Intermediate (FAI)1-x-PbI2 for Solar Cells. *Advanced Materials* 27(33):4918–4923.
17. Xu X, et al. (2018) Air-processed mixed-cation Cs0.15FA0.85PbI3 planar perovskite solar cells derived from a PbI2-CsI-FAI intermediate complex. *Journal of Materials Chemistry A* 6(17):7731–7740.
18. Sanchez S, Steiner U, Hua X (2019) Phase Evolution during Perovskite Formation - Insight from Pair Distribution Function Analysis. *Chemistry of Materials* 31(9):3498–3506.
19. Pradeesh K, Baumberg JJ, Prakash GV (2009) In situ intercalation strategies for device-quality hybrid inorganic-organic self-assembled quantum wells. *Applied Physics Letters* 95(3):033309.
20. Jain SM, et al. (2016) Vapor phase conversion of PbI2 to CH3NH3PbI3: spectroscopic evidence for formation of an intermediate phase. *Journal of Materials Chemistry A* 4(7):2630–2642.
21. Laio A, Parrinello M (2002) Escaping free-energy minima. *Proceedings of the National Academy of Sciences of the United States of America* 99(20):12562–12566.
22. Barducci A, Bussi G, Parrinello M (2008) Well-tempered metadynamics: A smoothly converging and tunable free-energy method. *Physical Review Letters* 100(2).
23. Que CJ, et al. (2017) Perovskite-Like Organic-Inorganic Hybrid Lead Iodide with a Large Organic Cation Incorporated within the Layers. *Inorganic Chemistry* 56(5):2467–2472.
24. Kamminga ME, de Wijs GA, Havenith RWA, Blake GR, Palstra TT (2017) The Role of Connectivity on Electronic Properties of Lead Iodide Perovskite-Derived Compounds. *Inorganic Chemistry* 56(14):8408–8414.
25. Lermer C, et al. (2018) Completing the Picture of 2-(Aminomethylpyridinium) Lead Hybrid Perovskites: Insights into Structure, Conductivity Behavior, and Optical Properties. *Chemistry of Materials* 30(18):6289–6297.
26. Stoumpos CC, Mao L, Malliakas CD, Kanatzidis MG (2017) Structure–Band Gap Relationships in Hexagonal Polytypes and Low-Dimensional Structures of Hybrid Tin Iodide Perovskites. *Inorganic Chemistry* 56(1):56–73.
27. Gratia P, et al. (2017) The Many Faces of Mixed Ion Perovskites: Unraveling and Understanding the Crystallization Process. *ACS Energy Letters* 2(12):2686–2693.
28. Ummadisingu A, Grätzel M (2018) Revealing the detailed path of sequential deposition for metal halide perovskite formation. *Science Advances* 4(2):e1701402.
29. Ummadisingu A, et al. (2017) The effect of illumination on the formation of metal halide perovskite films. *Nature* 545(7653):208–212.
30. Harms HA, Tetreault N, Pellet N, Bensimon M, Gratzel M (2015) Mesoscopic photosystems for solar light harvesting and conversion: facile and reversible transformation of metal-halide perovskites. *Faraday discussions* 176:251–269.
31. Leguy AMA, et al. (2016) Dynamic disorder, phonon lifetimes, and the assignment of modes to the vibrational spectra of methylammonium lead halide perovskites. *Phys. Chem. Chem. Phys.* 18(39):27051–27066.
32. Daub M, Hillebrecht H (2018) Tailoring the band gap in 3d hybrid perovskites by substitution of the organic cations: (ch3nh3)1-2y(nh3(ch2)2nh3)2ypb1-yi3 ($0 \geq y \leq 0.25$). *Chemistry – A European Journal* 24(36):9075–9082.
33. Warren RF, Liang WY (1993) Raman spectroscopy of new lead iodide intercalation compounds. *Journal of Physics: Condensed Matter* 5(35):6407–6418.
34. Pellegrino G, et al. (2016) From PbI2 to MAPbI3 through Layered Intermediates. *The Journal of Physical Chemistry C* 120(35):19768–19777.
35. Beckmann PA (2010) A review of polytypism in lead iodide. *Crystal Research and Technology* 45(5):455–460.
36. Khilji MY, Sherman WF, Wilkinson GR (1982) Raman study of three polytypes of pbi2. *Journal of Raman Spectroscopy* 13(2):127–133.
37. Zhang T, et al. (2019) Spontaneous low-temperature crystallization of α-fapbi3 for highly efficient perovskite solar cells. *Science Bulletin* 64(21):1608–1616.
38. Dutta NS, Noel NK, Arnold CB (2020) The crystalline nature of colloids in methylammonium lead halide perovskite precursor inks revealed by cryo-electron microscopy. *The Journal of Physical Chemistry Letters.*
39. Snaith HJ, Eperon GE, Ball JM (2020) Two-step deposition process.
40. Coleman C, et al. (1996) Intercalation of hydrazines in lead iodide. *Journal of Physics and Chemistry of Solids* 57(6):1153 – 1158. Proceeding of the 8th International Symposium on Intercalation Compounds.
41. Caddeo C, Saba MI, Meloni S, Filippetti A, Mattoni A (2017) Collective Molecular Mechanisms in the CH3NH3 PbI3 Dissolution by Liquid Water. *ACS Nano* 11(9):9183–9190.
42. Ryckaert JP, Ciccotti G, Berendsen HJ (1977) Numerical integration of the cartesian equations of motion of a system with constraints: molecular dynamics of n-alkanes. *Journal of Computational Physics* 23(3):327–341.
43. Plimpton S (1995) Fast Parallel Algorithms for Short-Range Molecular Dynamics. *Journal of Computational Physics* 117(1):1–19.
44. Bussi G, Donadio D, Parrinello M (2007) Canonical sampling through velocity rescaling. *The*

Journal of Chemical Physics 126(1):014101.
45. Parrinello M, Rahman A (1981) Polymorphic transitions in single crystals: A new molecular dynamics method. *Journal of Applied Physics* 52(12):7182–7190.
46. Tribello GA, Bonomi M, Branduardi D, Camilloni C, Bussi G (2014) PLUMED 2: New feathers for an old bird. *Computer Physics Communications* 185(2):604–613.
47. Giannozzi P, et al. (2009) QUANTUM ESPRESSO: a modular and open-source software project for quantum simulations of materials. *Journal of Physics: Condensed Matter* 21(39):395502.
48. Perdew JP, et al. (2008) Restoring the Density-Gradient Expansion for Exchange in Solids and Surfaces. *Physical Review Letters* 100(13):136406.
49. Perdew JP, Burke K, Ernzerhof M (1996) Generalized gradient approximation made simple. *Physical review letters* 77(18):3865.
50. Grimme S (2006) Semiempirical gga-type density functional constructed with a long-range dispersion correction. *Journal of computational chemistry* 27(15):1787–1799.
51. Niu H, Piaggi PM, Invernizzi M, Parrinello M (2018) Molecular dynamics simulations of liquid silica crystallization. *Proceedings of the National Academy of Sciences of the United States of America* 115(21):5348–5352.
52. Debye P (1915) Zerstreuung von Röntgenstrahlen. *Annalen der Physik* 351(6):809–823.
53. Ahlawat P, et al. (2019) Atomistic mechanism of the nucleation of methylammonium lead iodide perovskite from solution. *Chemistry of Materials* 32(1):529–536.
54. Oganov AR, Ono S (2004) Theoretical and experimental evidence for a post-perovskite phase of MgSiO3 in Earth's D" layer. *Nature* 430(6998):445–448.
55. Li Y, et al. (2018) A Perovskite Electrolyte That Is Stable in Moist Air for Lithium-Ion Batteries. *Angewandte Chemie International Edition* 57(28):8587–8591.
56. Ledinskyy M, et al. (2015) Raman spectroscopy of organic–inorganic halide perovskites. *The journal of physical chemistry letters* 6(3):401–406.
57. Sheng CX, et al. (2015) Laser action and photoexcitations dynamics in PbI2 films. *Optical Materials Express* 5(3):530–537.

Supplementary Information for

Molecular dynamics simulations of two-step process enable room-temperature synthesis of α-$FAPbI_3$

Paramvir Ahlawat, Haizhou Lu, Amita Ummadisingu, Haiyang Niu, Michele Invernizzi, Shaik Mohammed Zakeeruddin, Anders Hagfeldt*, Michael Graetzel*, Ursula Rothlisberger*, and Michele Parrinello*

This PDF file includes:

Supplementary text
Figs. S1 to S6

Supporting Information Text

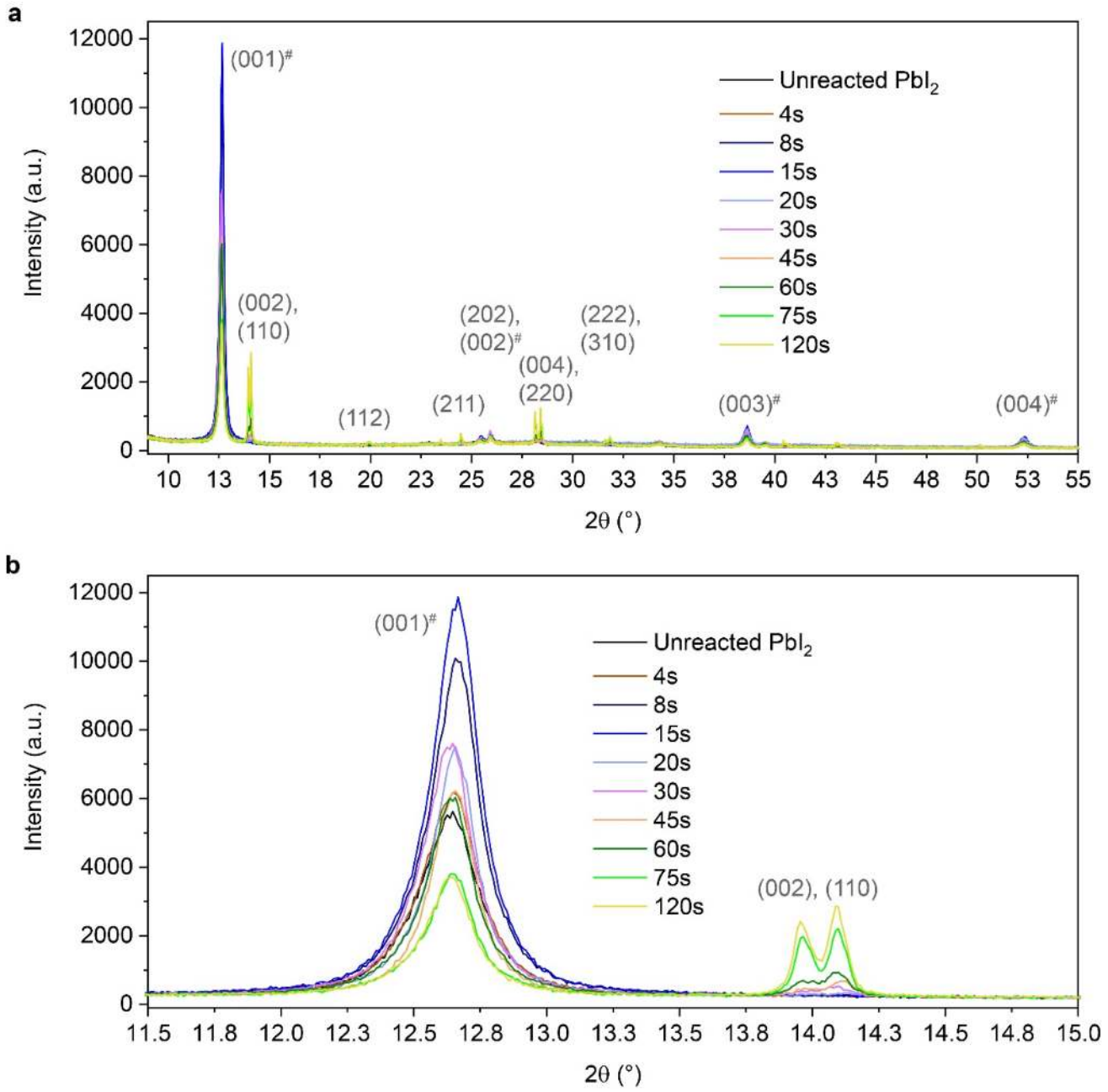

Fig. S1. XRD spectra monitoring the progress of $MAPbI_3$ formation in the sequential deposition reaction Plots show an unreacted PbI_2 sample and samples dipped in 5mgml^{-1} MAI solution for 4, 8, 15, 20, 30, 45, 60, 75 and 120s. Reflections of the PbI_2 in the 2H polytype are marked with # while the remaining peaks are assigned based on the tetragonal phase of the $MAPbI_3$. a) Full spectra showing all detected peaks. b) Zoom of a.

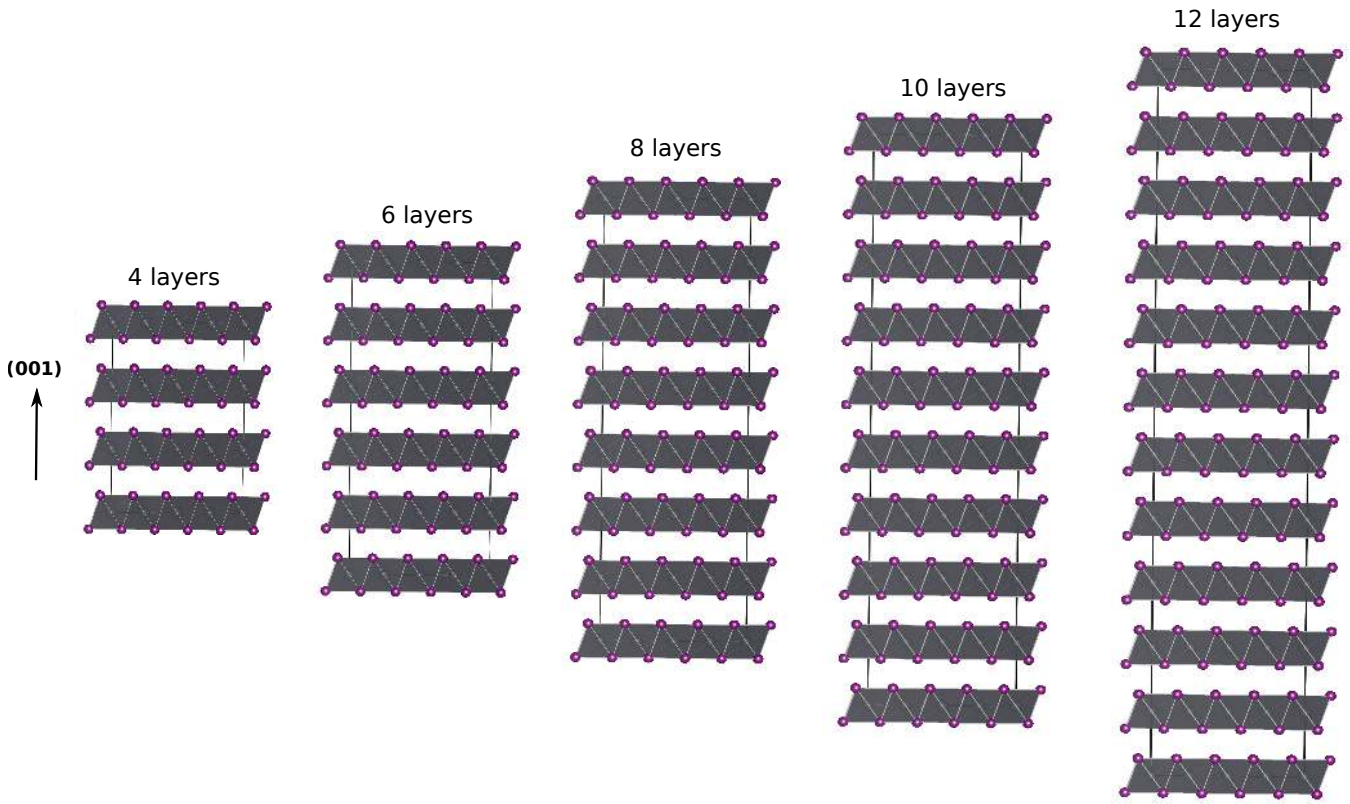

Fig. S2. PbI_2 supercells with different number of layers in (001) direction All supercells are represented with grey Pb-I octahedra with Pb in center and I at corners with pink spheres.

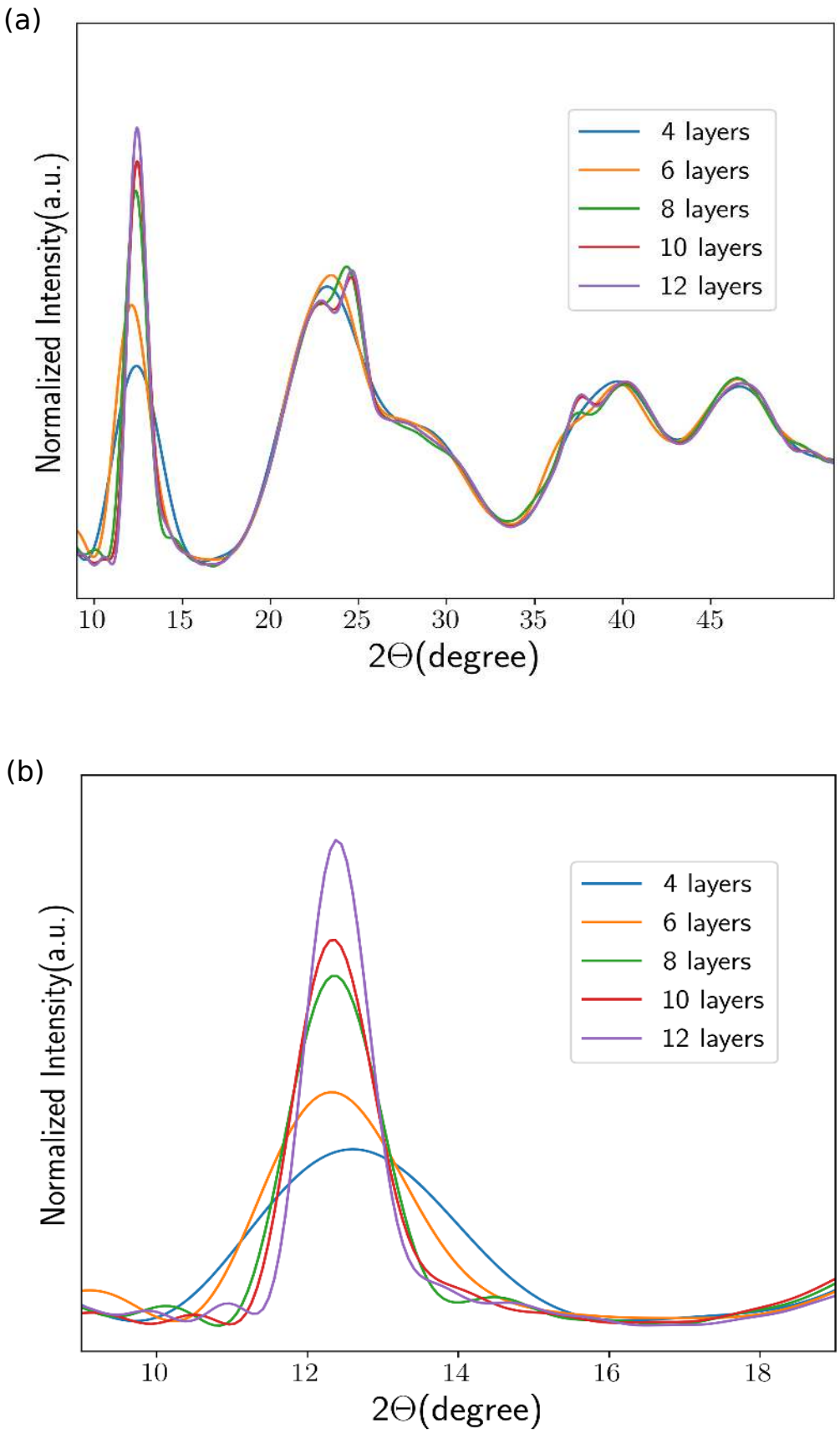

Fig. S3. Corresponding XRD spectra of different supercells depicted in Figure S2

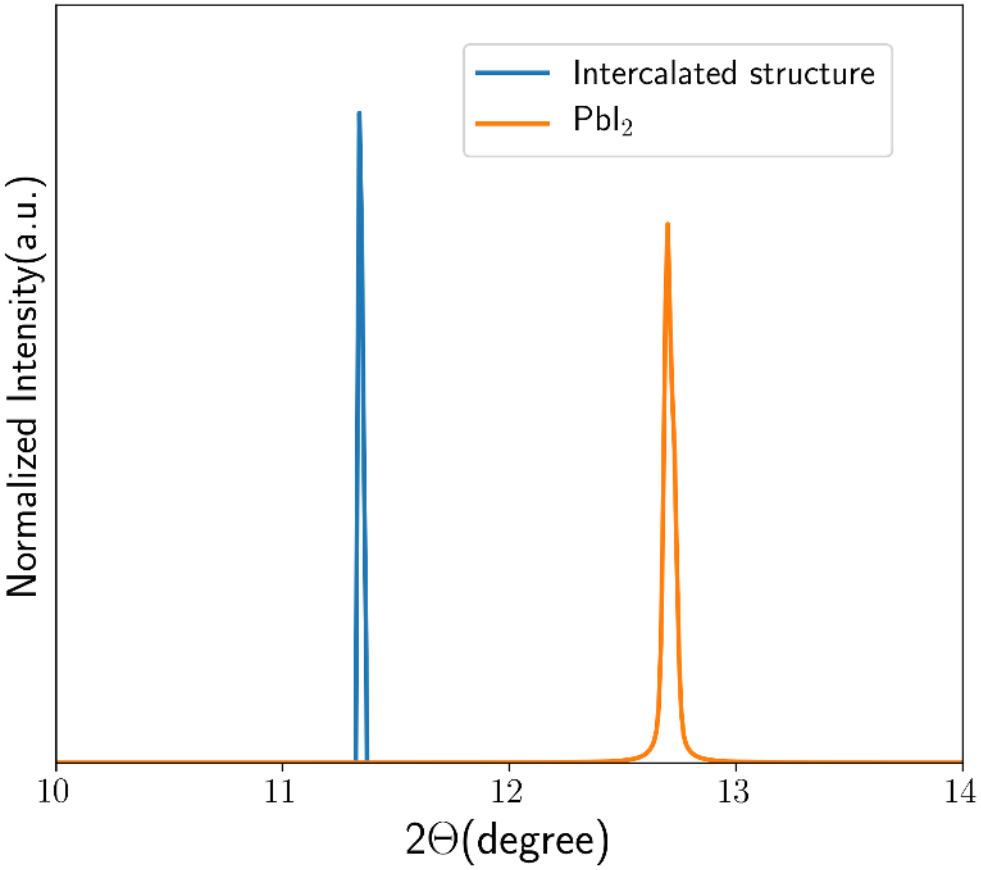

Fig. S4. Comparison of the first peak of powder diffraction patterns of DFT-D2 optimized PbI_2 and intercalated structure. We use VESTA software to calculate the powder diffraction patterns.

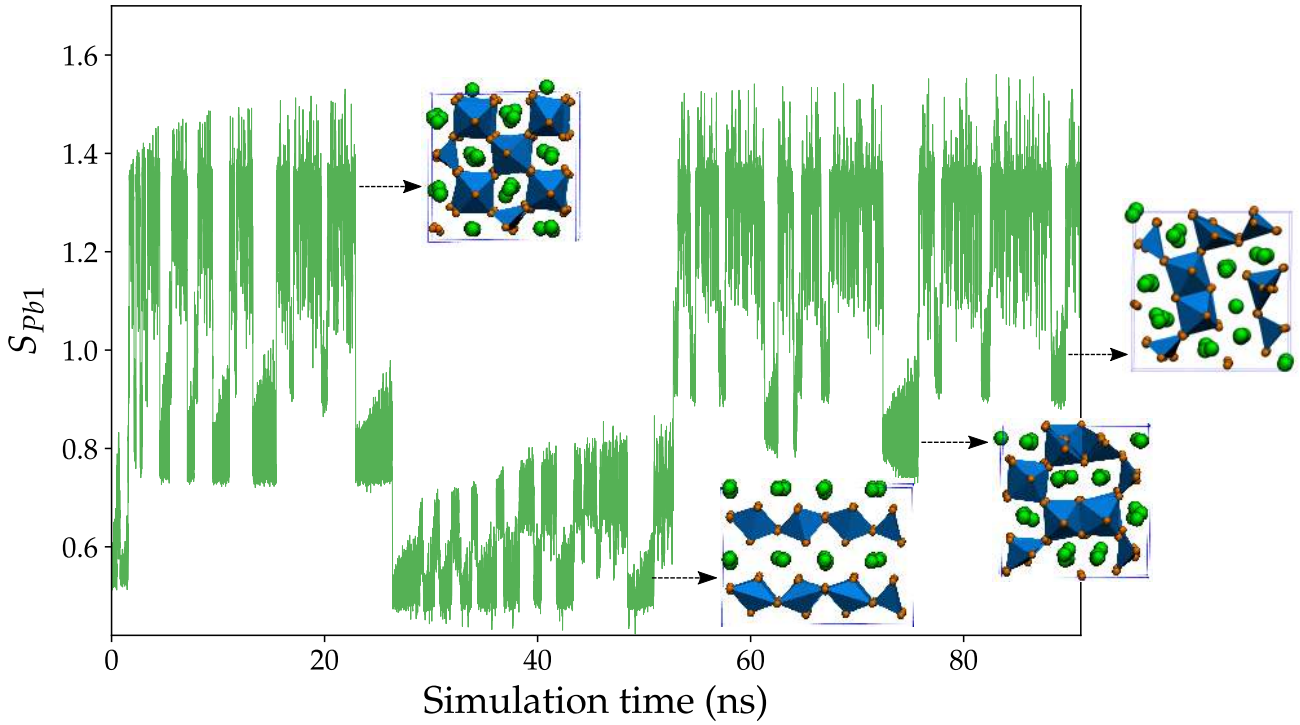

Fig. S5. Observed structures for $MAPbI_3$ for smaller supercell. Pb-I complexes are shown as golden polyhedra with Pb^{2+} in the center and I^- on the corners. Free I^- is shown as pink spheres. MA^+ ions are shown with ball and sticks with carbon as light blue, nitrogen as dark blue and hydrogens being white.

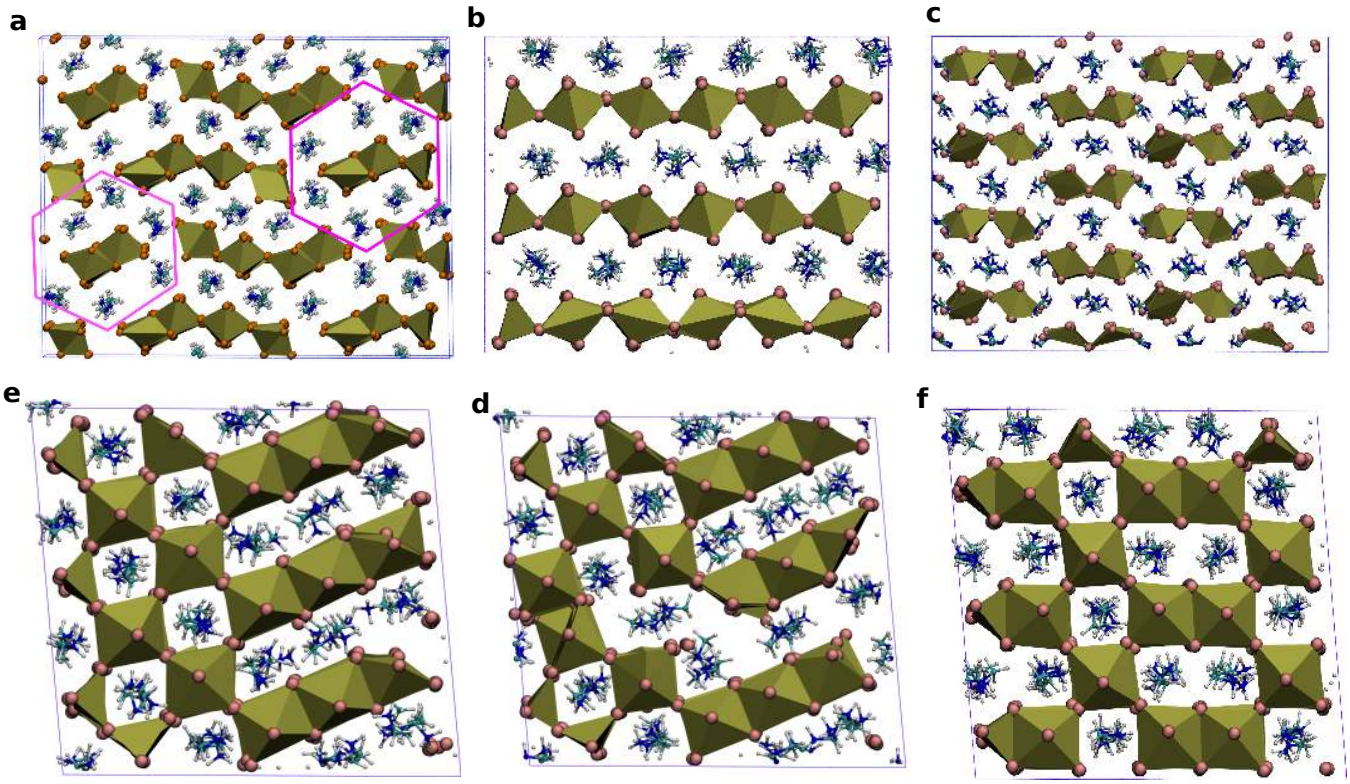

Fig. S6. Different polymorphs: Pb-I complexes are shown as golden polyhedra with Pb^{2+} in the center and I^- on the corners. Free I^- is shown as pink spheres. MA^+ ions are shown with ball and sticks with carbon as light blue, nitrogen as dark blue and hydrogens being white. Hexagons are drawn in figure (a) to show the similarity to the solvent intercalated 1D phases during crysatllization of halide perovskites.